SCIENCE CHINA

Technological Sciences



Article

April 2024 Vol.67 No.4: 1124–1132 https://doi.org/10.1007/s11431-023-2589-3

Sparse identification-assisted exploration of the atomic-scale deformation mechanism in multiphase CoCrFeNi high-entropy alloys

XIAO Lu¹, GUO XiaoXiang¹, SUN YuTong², WANG Gang³, LONG WeiMin⁴, LIAW Peter K.⁵ & REN JingLi^{1*}

School of Mathematics and Statistics, Zhengzhou University, Zhengzhou 450001, China;
 Academy of Mathematics and Systems Science, Chinese Academy of Sciences, Beijing 100190, China;
 Institute of Materials, Shanghai University, Shanghai 200444, China;
 SKL of Advanced Brazing Metals & Technology, Zhengzhou Research Institute of Mechanical Engineering, Zhengzhou 450001, China;
 Department of Materials Science and Engineering, The University of Tennessee, Knoxville, TN 37996, USA

Received October 20, 2023; accepted January 4, 2024; published online March 21, 2024

This study investigated the atomic-scale deformation mechanism of multiphase CoCrFeNi high-entropy alloys (HEAs) at liquid helium, liquid nitrogen, and room temperatures. A million-atom multiphase HEA was prepared using molecular dynamics simulation involving melt and quench processes. The HEA exhibited high-density dislocations and some twins, consistent with experimental observations. Quantitative analysis revealed an inconsistent evolution of the microstructure under tensile deformation. In particular, the elastic and initial plastic stages exhibited an increase in the disordered structure at the expense of the face-centered cubic and hexagonal close-packed structures, followed by a subsequent transformation involving multiple structural rearrangements. Furthermore, through sparse identification, a model depicting microstructural evolution during tension was extracted for the CoCrFeNi HEA at three typical temperatures and three tensile rates. The model highlighted the importance of the body-centered cubic structure in the evolutionary process.

high-entropy alloy, data-driven method, microstructure evolution, multiphase structure, molecular dynamics simulation

Citation: Xiao L, Guo X X, Sun Y T, et al. Sparse identification-assisted exploration of the atomic-scale deformation mechanism in multiphase CoCrFeNi high-entropy alloys. Sci China Tech Sci, 2024, 67: 1124–1132, https://doi.org/10.1007/s11431-023-2589-3

1 Introduction

High-entropy alloys (HEAs), initially defined by Yeh et al. [1] and termed multicomponent alloys by Cantor et al. [2], are solid-solution alloys containing principal elements with equal or nearly equal atomic percentages. These alloys exhibit numerous outstanding mechanical properties, such as high yield strength, ultrahigh hardness, and excellent wear resistance [3–6]. Thus, they have drawn extensive attention from both academia and engineering fields [7–10].

centered cubic (BCC), or disordered structures [11–13]. However, owing to limitations in experimental techniques, directly observing the atomic-scale structural evolution during deformation is challenging. Molecular dynamics (MD) simulations, involving the use of classical Newton's equations to compute object trajectories, offer a means to continuously and directly visualize atomic behavior during deformation simulations [14–16]. Several pioneering studies have investigated HEAs through MD simulations. For instance, Li et al. [17] investigated the impacts of chemical

HEAs typically manifest solid-solution phases with facecentered cubic (FCC), hexagonal close-packed (HCP), body-

^{*}Corresponding author (email: renjl@zzu.edu.cn)

order and solute segregation on grain boundary migration in NbMoTaW HEAs. Similarly, Chen et al. [18] explored the influence of atomic segregation and short-range ordering on the melting temperature of HEAs. Giwa et al. [19] explored theories related to low-temperature strengthening and assessed their performance regarding the temperature-dependent size effect and work hardening in Al_{0.7}CoCrFeNi HEAs.

This investigation of nanomaterial microstructures has significantly elucidated plastic deformation. Numerous studies on HEAs have concentrated on single-phase structures owing to the ease of observing their deformation behavior visually. While in practical laboratory or engineering applications, most HEAs consist of multiple phases [20,21]. For example, a CoCrFeNi HEA prepared in an experiment showed an FCC-phase-dominated crystalline structure with some twins and high-density dislocations [21]. In earlier MD simulations, multiphase HEAs were often created through the artificial introduction of multiple nanotwins, where the dislocations and twins do not interact with any defects other than grain boundaries [7,22,23]. In reality, the spontaneous formation of multiphase HEAs is achieved through melting and quenching simulations [24–26]. However, capturing the microstructural evolution of multiphase HEAs during deformation solely through visualization is not straightforward. Consequently, we are intrigued by the microstructure evolution mechanism in multiphase HEAs under tensile deformation.

In addition to the inherent limitations of visual analysis, there remains a lack of systematization and thoroughness in handling the vast amount of data generated by experiments or simulations. Data mining methods offer a means to uncover hidden physical and mechanistic mechanisms from numerous data, thereby facilitating advancements in materials science [27–32]. Recently, researchers have explored the application of sparse identification techniques to extract nonlinear dynamics within systems. The advantage of the sparse identification algorithm lies in its ability to automatically unveil physical laws, making it well-suited for investigating the evolution mechanisms of microstructures [29,33]. Moreover, the derived explicit expressions overcome the limitations of the black-box model, which are difficult to interpret.

In this study, MD simulation and sparse identification techniques are combined to investigate the microstructural evolution of multiphase HEAs during tensile deformation at different temperatures. Tensile simulations were conducted on a representative HEA, that is, the CoCrFeNi alloy, at three typical temperatures [21]: room temperature (300 K), liquid nitrogen temperature (77 K), and liquid helium temperature (4.2 K), under different tensile rates: 5×10^8 , 1×10^9 , and 1×10^{10} s⁻¹ [7,24,25]. The overall strategy flowchart for exploring the atomic-scale deformation mechanism in multiphase CoCrFeNi HEA is illustrated in Figure 1.

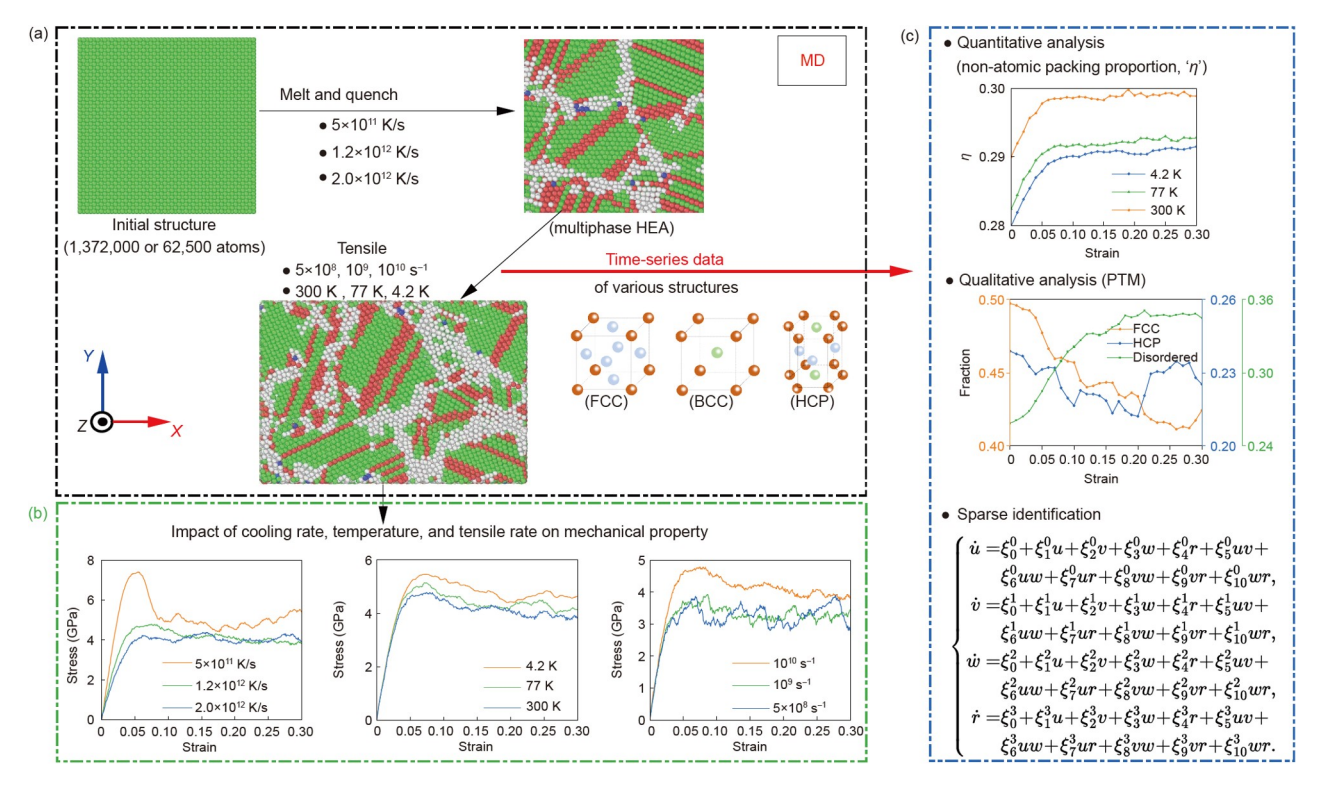


Figure 1 Strategy flowchart illustrating the exploration of the atomic-scale deformation mechanism of multiphase CoCrFeNi HEAs. (a) Preparation of the multiphase HEA and MD simulation of tensile deformation. (b) Effects of cooling rate, temperature, and tensile rate on mechanical properties. (c) Structural evolution exploration by quantitative, qualitative, and sparse identification based on time-series data obtained from MD simulation.

2 Results and discussion

2.1 Experimental details

All simulations were conducted using the Large-scale Atomic/Molecular Massively Parallel Simulator (LAMMPS) code [34]. The initial sizes of the CoCrFeNi HEAs comprised 1372000 atoms and 62500 atoms, occupying volumes of 24.78 nm \times 24.78 nm \times 24.78 nm and 8.85 nm \times 8.85 nm × 8.85 nm, respectively. To generate polycrystalline samples (Figure 2(a)), MD simulations of melt and quench were employed. The detailed process is as follows: (a) Atoms randomly distributed in the FCC lattice are heated to 3000 K and equilibrated at 3000 K to create a homogeneous liquid under the isothermal-isobaric (NPT) ensemble. (b) Subsequently, the liquid is quenched to three temperatures (300, 77, and 4.2 K) at three different cooling rates and then relaxed until equilibrium conditions. HEAs were subjected to uniaxial tensile deformation along the X-axis at three typical strain rates: 5×10^8 , 1×10^9 , and 1×10^{10} s⁻¹, respectively [7,24,25]. Periodic boundary conditions were applied in all directions. The atomistic force was computed using the embedded atom method (EAM) potential developed by Farkas and Caro [35], widely employed in the MD community to investigate the deformation behavior of CoCrFeNi HEAs [36–38]. In addition, ref. [39] revealed that the stacking fault energy of CoCrFeNi HEAs calculated using this potential was comparable to that of a previous study [6]. The lattice structure and distortion were determined through polyhedral template matching (PTM) [40] and dislocation analysis (DXA) [41] within the visualization software Open Visualization Tool (OVITO) [42]. Different types of atoms are visually distinguished by color: green, red, blue, and white correspond to FCC, HCP, BCC, and disordered structures, respectively. Disordered atoms are those that cannot be identified by any crystalline order [43].

Studies have highlighted the significant influence of cooling rates on microstructural phase formation during solidification. For instance, Li et al. [24] demonstrated that a cooling rate lower than 5×10^{12} K/s resulted in crystallization. Sharma and Balasubramanian [25] showed that an

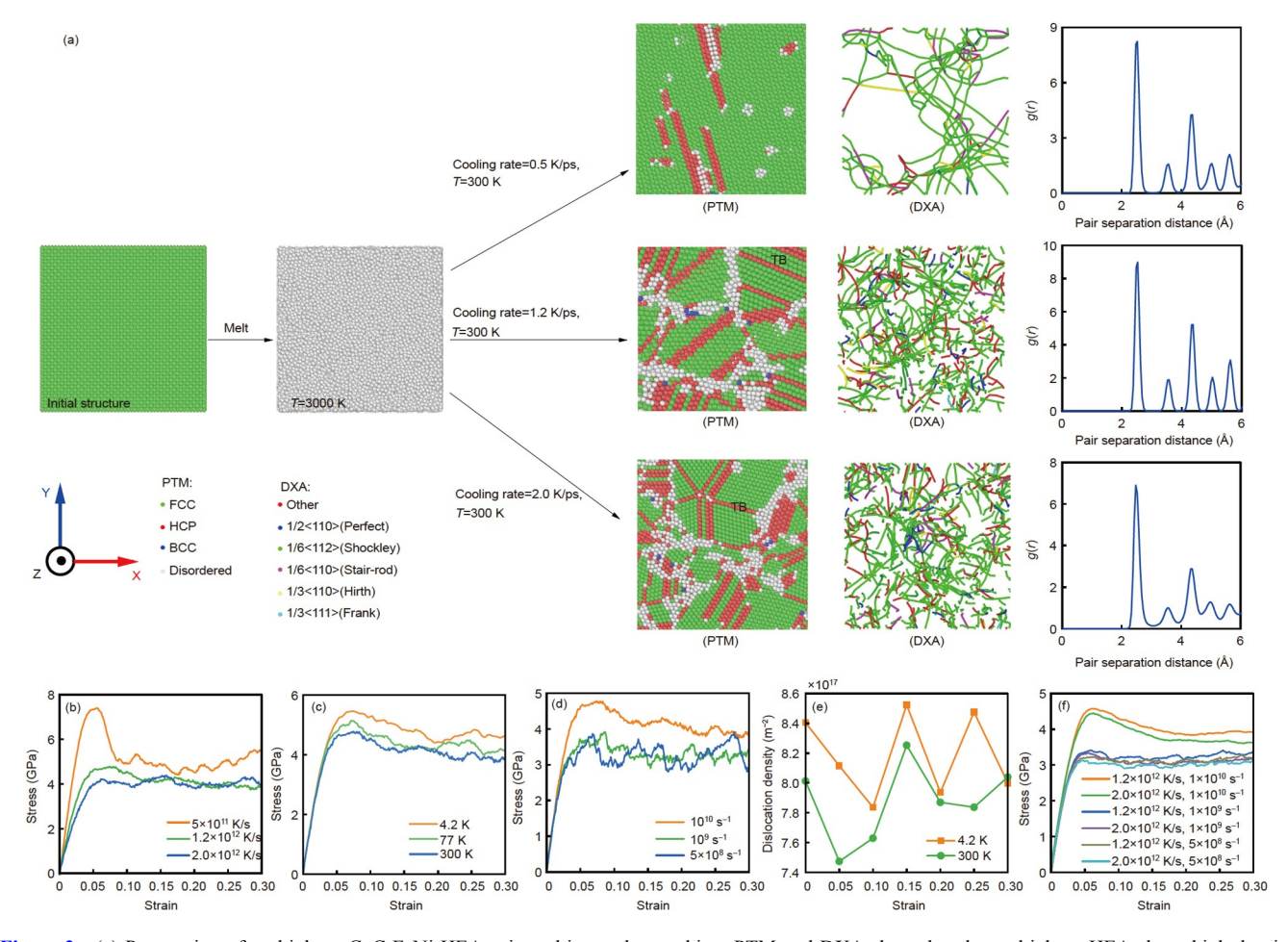


Figure 2 (a) Preparation of multiphase CoCrFeNi HEAs via melting and quenching. PTM and DXA show that the multiphase HEAs have high-density dislocations and some twins; the radial pair distribution functions, g(r), exhibit typical FCC phase-dominated crystalline structures. (b)–(d) Stress–strain curves of small-sized HEA under different cooling rates, temperatures, and tensile rates, respectively. (e) Variation of dislocation density with strain at 300 and 4.2 K. (f) Stress–strain curves of large-sized HEA under different cooling and tensile rates.

HEA prepared at a cooling rate of 4.5×10^{11} K/s exhibited a typical FCC lattice. Thus, cooling rates of 5×10^{11} , 1.2×10^{11} 10^{12} , and 2×10^{12} K/s were employed to prepare multiphase CoCrFeNi HEA. Table 1 presents a breakdown of the fractions of different crystal structures for samples of two sizes. The data indicate that the final crystal structure remains largely unaffected by size and is primarily influenced by the cooling rate. Therefore, considering computational capacity and cost, HEAs composed of 1372000 atoms were prepared at a temperature of 300 K and cooled at rates of 1.2×10^{12} and 2×10^{12} K/s, respectively. Furthermore, common neighbor analysis (CNA) [44] revealed structural fractions of 46.52% for FCC, 20.90% for HCP, 2.20% for BCC, and 30.37% for disordered structures at 300 K with a cooling rate of 1.2×10^{12} K/s. These findings slightly differ from the results acquired via PTM. Considering that PTM uses Voronoi polyhedra to determine neighbors, it is more reliable than CNA in the structural identification of HEA.

The results of PTM, DXA, and the radial pair distribution function (g(r)) for the undeformed alloy are depicted in Figure 2(a). The g(r) values, derived from the average of all atomic pairs, indicate that the prepared HEAs predominantly exhibited typical FCC phase-dominated crystal structures. Here, a single layer comprising HCP atoms was identified as a twin boundary [25]. A comparison of the analysis results from PTM and DXA across different cooling rates revealed that HEAs prepared at higher cooling rates exhibited higherdensity dislocations and some twins, aligning with previous experimental findings [21]. Furthermore, as illustrated in Figure 2(b), a lower cooling rate resulted in significant softening. Hence, our focus was on investigating the deformation behavior under cooling rates of 1.2×10^{12} and 2×10^{12} 10¹² K/s. The effects of temperature and tensile rate on the tensile properties of the multiphase CoCrFeNi HEA are presented in Figure 2(c) and (d), respectively. For all simulations, the stress increased linearly with strain during the initial elastic stage (<2%), then almost linearly with strain until the yield point, and finally exhibited a serrated flow with increasing strain. The yield strength increased with decreasing temperature or increasing tensile rate, consistent with the results of previous studies [21,45]. The dislocation itself is an effective obstacle to dislocation movement, leading to strengthened materials. Hence, the variation in dislocation density (ρ) with strain at 300 and 4.2 K was studied (Figure 2(e)). Here, $\rho = L/V$, where L is the total length of the dislocation lines, and V is the volume of the simulation sample. This indicates that as temperature decreased, the dislocation density increased. Comparatively, at lower temperatures, the movement of dislocations became hindered, leading to an increase in yield strength with decreasing temperature. Furthermore, the fluctuation in dislocation density evolution with increased loading illustrates that dislocation annihilation contributes to the serration observed in stress-strain behavior [25]. The larger sample exhibited similar results (Figure 2(f)). To streamline the paper's length, this study focused on the scenario involving a cooling rate of 1.2×10^{12} K/s and a tensile rate of 1×10^{10} s⁻¹. The outcomes from other cases and a summary of the deformation conditions are presented in the Supporting information.

2.2 Nonatomic packing proportion

The nonatomic packing proportion, denoted as η in this work, represents the ratio of the region unoccupied by atoms in the CoCrFeNi HEA. The η is computed using Delaunay triangulation, which decomposes the entire model into N disjoint tetrahedra according to the atomic coordinates. As depicted in Figure 3(a), the dark blue and white sections of the resulting tetrahedra represent the volume occupied by atoms and the volume unoccupied by atoms, respectively. Thus, $\eta = \sum V_{\text{non-atom}} / \sum V_{\text{tetrahedron}}$, where $V_{\text{tetrahedron}}$ and $V_{\text{non-atom}}$ represent the volume of a tetrahedron and the volume occupied by nonatoms, respectively. A detailed calculation procedure is available in the Supporting information.

Unlike existing qualitative parameters (e.g., PTM) that identify local lattice features on the atomic scale, η is a quantitative metric. According to the atomic packing factors (APFs), the η is 0.26 for the FCC structure (APF = 0.74) but 0.32 for the BCC structure (APF = 0.68). Consequently, any structural rearrangement during tensile deformation will result in a change in the η value. Thus, in multiphase HEAs, analyzing the evolution of η with strain aids in understanding microstructural changes. As depicted in Figure 3(b), η demonstrates an inconsistent evolution trend during tension.

Table 1 PTM and CNA for quenched HEAs

HEA	Method	Cooling rate (K/s)	FCC	НСР	BCC	Disordered	
		5×10^{11}	77.39%	18.02%	0.03%	4.56%	
(2500	PTM	1.2×10^{12}	49.73%	23.89%	0.52%	25.86%	
62500 atoms		2.0×10^{12}	45.81%	23.29%	1.35%	29.55%	
	CNA	1.2×10^{12}	46.53%	20.90%	2.20%	30.37%	
1272000	DTM	1.2×10^{12}	46.75%	25.36%	1.13%	26.76%	
1372000 atoms	PTM	2.0×10^{12}	43.40%	22.95%	1.34%	32.31%	

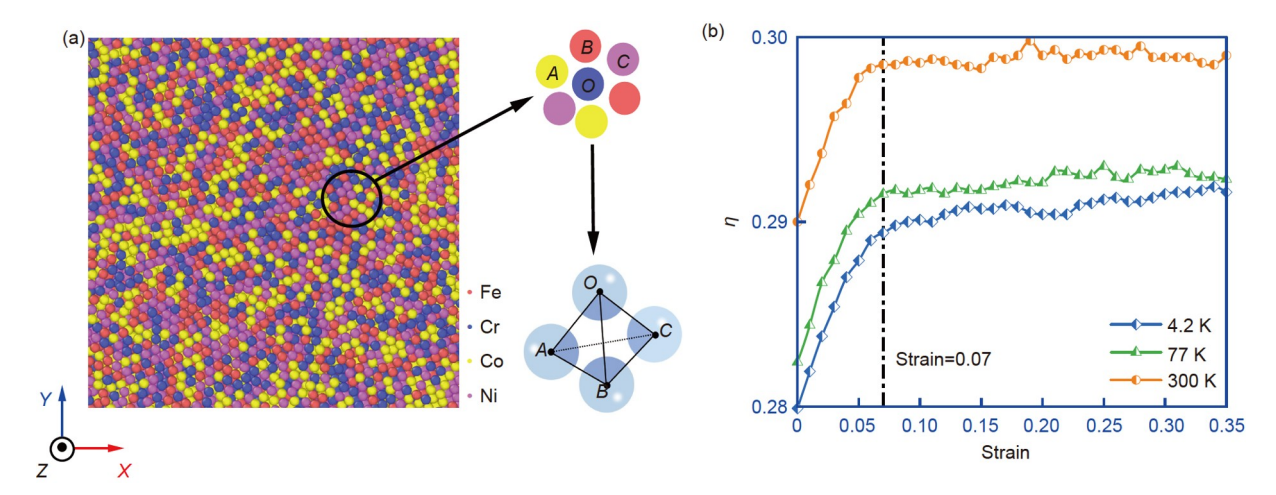


Figure 3 (Color online) (a) Nonatomic packing proportion. The deep blue and white colors in the tetrahedron represent the atomic-occupied and nonatomic-occupied volumes, respectively. (b) Nonatomic proportion versus strain at 300, 77, and 4.2 K.

Initially, it shows a nearly linear increase with strain in the elastic and initial plastic stages, followed by a serrated evolution in the subsequent stage, with the turning point occurring at \sim 7% strain. This highlights an intense competition among various structures during the initial tensile deformation. The competition gradually stabilizes as the deformation progresses.

2.3 Microstructural evolution analysis

To explore the inconsistent structural evolution trend, we visually analyze time-series data of various structural fractions obtained using the PTM method. According to Figure 4 (a), the microstructural evolution at 300 K can be segmented into several stages based on turning points. Initially, when the strain is below 7%, the disordered structure increases at the expense of the FCC and HCP structures. Subsequently, the evolution trend of the FCC structure briefly stabilizes, during which the disordered structure mainly increases at the expense of the HCP structure. Following this stage, the evolution trends of the FCC and HCP structures become opposite, with the disordered structure continuously increasing and gradually stabilizing. A similar phenomenon occurred at 77 K (Figure 4(b)). However, the evolution trend at 4.2 K is different. As depicted in Figure 4(c), when the strain is below 9%, the disordered structure increases at the expense of the FCC and HCP structures. Subsequently, the evolution trend of the HCP structure briefly reaches a steady state, during which the rise in disordered structure primarily occurs at the expense of the FCC structure. Following this stage, after a brief stabilization in the evolution trend of the FCC structure, the trends of the FCC and HCP structures become opposite, with the disordered structure continuously increasing and gradually stabilizing.

These results suggest that the inconsistency in micro-

structural evolution is characterized by the rise in disordered structures, leading to a reduction in FCC and HCP structures during the elastic and initial plastic stages. Consequently, the evolution trend of the FCC or HCP structures briefly stabilizes. Subsequently, the trends for the FCC and HCP structures become opposite, while the disordered structure gradually stabilizes.

2.4 Mathematical equation extraction

In our MD simulation, we initially generate the multiphase HEA via melt and quench processes, resulting in high-density dislocations and some twins, consistent with experimental observations [21]. Subsequently, we conduct the tensile tests at three typical temperatures and three different tensile rates, collecting time-series data of various structures during the tension process through PTM analysis. Considering the complexities in uncovering underlying knowledge solely through visualization of time-series data, we employ sparse identification, a data-driven method renowned for its efficacy in information mining [29,33]. Thus, we integrate the time-series data obtained from the MD simulation with sparse identification to explore the evolutionary mechanism of microstructure. Our approach involves establishing a mathematical equation through sparse identification using diverse structural time-series data, enabling the exploration of atomic-scale deformation behavior. For a comprehensive understanding, a detailed strategy flowchart is provided in Figure 1. The extracted differential equation system is represented as follows:

$$\dot{\mathbf{X}}(t) = f(\mathbf{X}(t)),\tag{1}$$

where the vector $\mathbf{X}(t) \in \mathbb{R}^n$ represents the state of the dynamic system at time t, and the nonlinear function f maps the dynamic state vector to the experimentally observable value

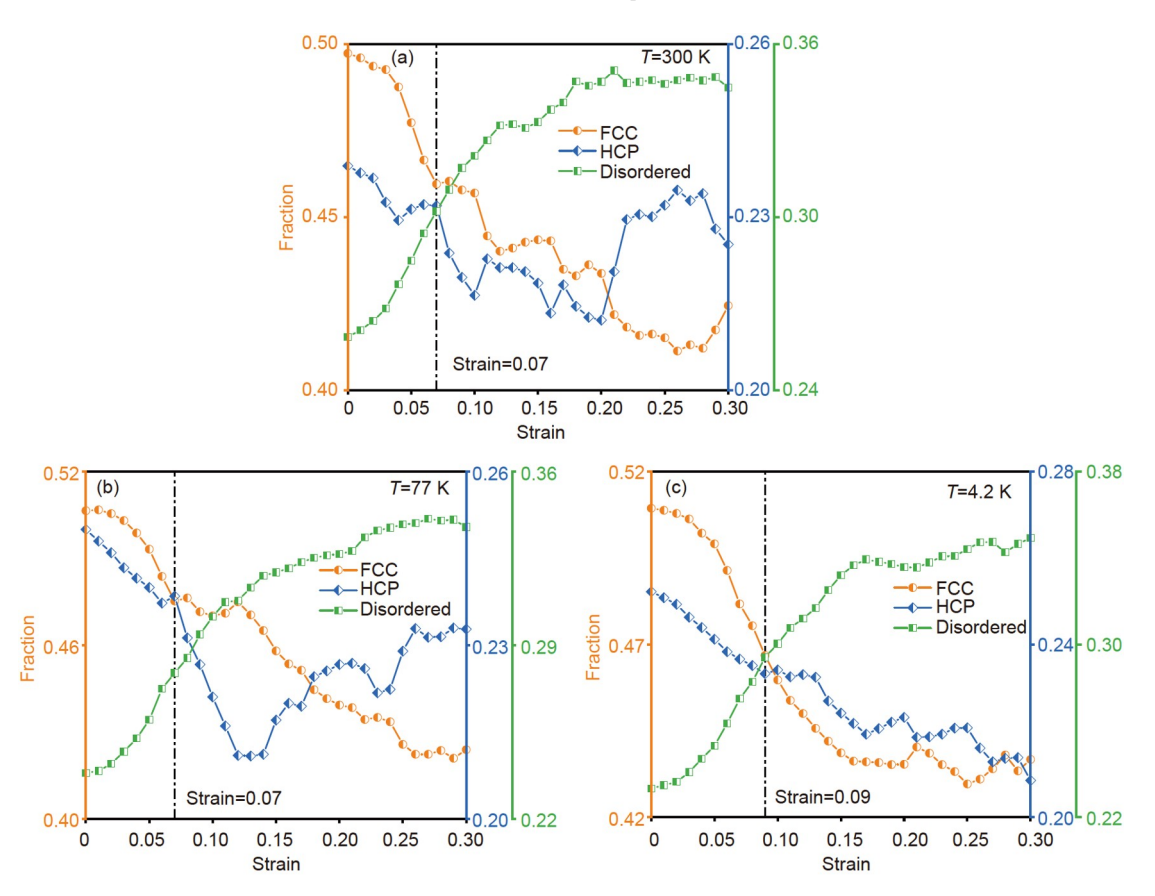


Figure 4 (Color online) Evolution tendency of various structural fractions with strain at different temperatures: (a) 300, (b) 77, and (c) 4.2 K.

[33].

As described in refs. [29,33], the system can be rewritten as follows:

$$\dot{\mathbf{X}}(t) = f(\mathbf{X}(t)) = \Theta(\mathbf{X})\mathbf{\Xi},\tag{2}$$

where $\Theta(\mathbf{X}) = [\theta_1(\mathbf{X}), \theta_2(\mathbf{X}), ..., \theta_n(\mathbf{X})]$ represents a basic library consisting of linear and nonlinear candidate functions, and $\mathbf{\Xi} = [\xi_1, \xi_2, ... \xi_n]$ is the sparse coefficient vector of the candidate functions to be determined. Each column of $\Theta(\mathbf{X})$ represents a candidate function. Thus, the extracted model for a small-sized HEA at 300 K and a tensile rate of 1 × 10^{10} s⁻¹ is defined as

$$\begin{cases} \dot{u} = \xi_{0}^{0} + \xi_{1}^{0}u + \xi_{2}^{0}v + \xi_{3}^{0}w + \xi_{4}^{0}r + \xi_{5}^{0}uv + \xi_{6}^{0}uw + \\ \xi_{7}^{0}ur + \xi_{8}^{0}vw + \xi_{9}^{0}vr + \xi_{10}^{0}wr, \\ \dot{v} = \xi_{0}^{1} + \xi_{1}^{1}u + \xi_{2}^{1}v + \xi_{3}^{1}w + \xi_{4}^{1}r + \xi_{5}^{1}uv + \xi_{6}^{1}uw + \\ \xi_{7}^{1}ur + \xi_{8}^{1}vw + \xi_{9}^{1}vr + \xi_{10}^{1}wr, \\ \dot{w} = \xi_{0}^{2} + \xi_{1}^{2}u + \xi_{2}^{2}v + \xi_{3}^{2}w + \xi_{4}^{2}r + \xi_{5}^{2}uv + \xi_{6}^{2}uw + \\ \xi_{7}^{2}ur + \xi_{8}^{2}vw + \xi_{9}^{2}vr + \xi_{10}^{2}wr, \end{cases}$$

$$\dot{r} = \xi_{0}^{3} + \xi_{1}^{3}u + \xi_{2}^{3}v + \xi_{3}^{3}w + \xi_{4}^{3}r + \xi_{5}^{3}uv + \xi_{6}^{3}uw + \\ \xi_{7}^{3}ur + \xi_{8}^{3}vw + \xi_{9}^{3}vr + \xi_{10}^{3}wr, \end{cases}$$

$$(3)$$

where the coefficients $\left\{\xi_{j}^{j}\right\}$ are sparse, u(t), v(t), w(t), and r(t)

represent the fractions of the FCC, HCP, BCC, and disordered structures at tensile time *t*, respectively. More detailed procedures are presented in the Supporting information.

For the small sample at 300 K and 1×10^{10} s⁻¹ tensile rate, Figure 5(a) compares the modeling results obtained from the model and the true time-series data. The well-fitted results validate the effectiveness of the extracted model in describing structural evolution. We conduct tensile simulations under 24 different cases, as outlined in Table S1. To further demonstrate the accuracy of this method, we derive models using the same foundational library $(\Theta(X))$ under the other 23 cases. Specifically, the 23 cases consist of 17 (=3 \times 2 \times 3 – 1) for small-sized HEA and 6 (= $1 \times 2 \times 3$) for big-sized HEA. Here, the notation $3 \times 2 \times 3$ denotes three temperatures, two cooling rates, and three tensile rates for small samples, and -1 refers to the case under consideration. Similarly, $1 \times 2 \times 3$ refers to one temperature, two cooling rates, and three tensile rates for large samples. The fitting result for the large-size sample at 300 K, a tensile rate of 1 × $10^{10} \,\mathrm{s}^{-1}$, and a cooling rate of $1.2 \times 10^{12} \,\mathrm{K/s}$ is shown in Figure 5(b), while the fitting results for other cases are shown in the Supporting information. According to the same basic library, the extracted models under various conditions effectively capture their respective microstructural evolutions,

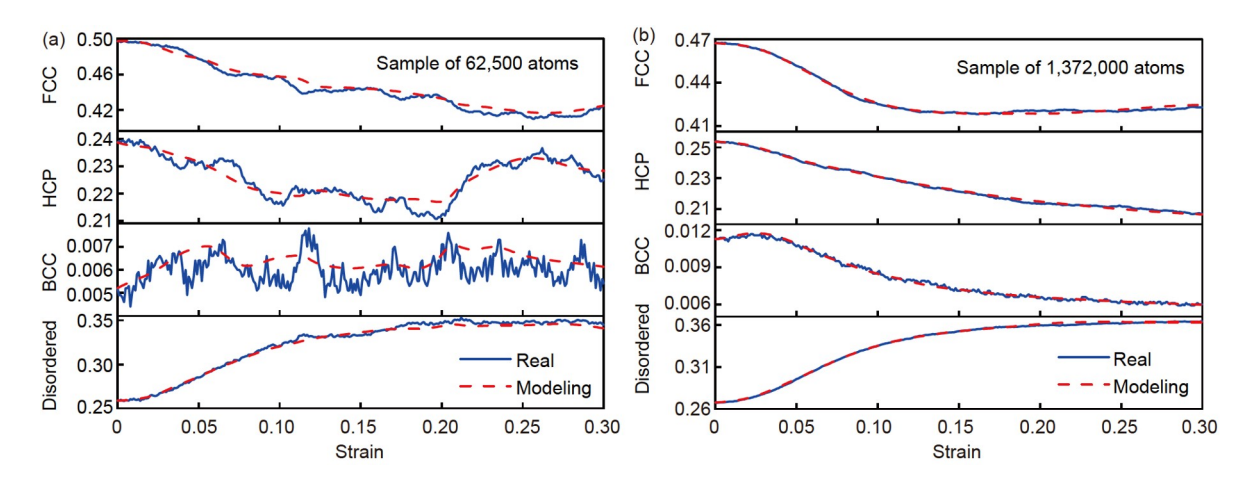


Figure 5 (Color online) Comparison of the structural fractions and modeling results of the prepared CoCrFeNi HEAs. (a) Small sample with 62500 atoms and (b) large sample with 1372000 atoms.

Table 2 Corresponding coefficients of the identified equations under a cooling rate of 1.2×10^{12} K/s, a tensile rate of 1×10^{10} s⁻¹, and temperatures of 300, 77, and 4.2 K

77, and 4.2 K													
$1.2 \times 10^{12} \text{ K/s}, 1 \times 10^{10} \text{ s}^{-1}$		1	и	ν	w	r	uv	uw	ur	vw	vr	wr	
62500 atoms		ù	-20.15	0	0.67	32.05	0.17	0	0	0	-1.07	0	-0.27
	200 K	\dot{v}	74.11	-0.89	-3.20	-28.04	-0.72	0.04	0	0	0.88	0.03	0.27
	300 K	ŵ	8.15	-0.09	-0.07	-15.56	-0.09	0	0.16	0	0.13	0	0.16
		r	37.14	-0.1	0.12	-93.23	-0.56	-0.02	0.87	0	1.08	0	0.94
	77 K	ù	-4.65	0	0.20	7.69	0	0	0	0	-0.34	0	0
		\dot{v}	7.22	0	-0.24	-13.07	-0.05	0	0	0	0.43	0	0.10
		ŵ	-3.61	0.04	0.03	5.33	0.03	0	-0.06	0	-0.04	0	-0.05
		r	-0.06	0	0	5.60	0	0	-0.05	0	-0.07	0	-0.06
	4.2 K	ù	68.38	-0.63	-0.83	-103.43	-0.66	0	0.97	0	1.2	0	1.00
		\dot{v}	-42.36	0.47	0.34	65.01	0.42	0	-0.74	0	-0.50	0	-0.64
		ŵ	1.83	-0.03	0	-2.89	-0.02	0	0.05	0	-0.02	0	0.03
		\dot{r}	12.58	-0.18	0	-15.88	-0.14	0	0.23	0	0	0	0.19
HEA with 1372000 atoms	300 K	ù	29.72	-0.33	-0.28	-35.43	-0.27	0	0.38	0	0.36	0	0.31
		\dot{v}	11.06	-0.10	-0.12	-17.42	-0.12	0	0.17	0	0.18	0	0.18
		ŵ	9.58	-0.10	-0.10	-14.52	-0.09	0	0.15	0	0.15	0	0.14
		ŕ	-6.10	0.08	0.04	3.48	0.04	0	-0.04	0	-0.05	0	0

confirming the feasibility of this method. Additionally, the structural evolution trend in the small sample appears less smooth compared with that in the large sample. This discrepancy is primarily attributed to the abundant presence of small grains in the small sample and their pronounced interaction across boundary conditions.

The coefficients of the identified mathematical equations under various conditions are presented in Table 2. Notably, the coefficient of the *w* term is higher than those of other linear terms, while the coefficients of quadratic terms without *w* exhibit sparsity. These results reflect the leading role of the BCC structure in structural evolution. In addition, all

coefficients of the *ur* term are equal to zero at different temperatures and samples, revealing a universal intrinsic mechanism in these cases. The same results can be found for other conditions (see Supporting information), indicating that the extracted model is somewhat generalizable.

The integration of MD simulation and sparse identification offers a computational avenue to explore the mechanical behavior of the multiphase CoCrFeNi HEA. Unlike conventional visual analysis tools, this approach can elucidate implicit internal mechanisms. Moreover, the proposed explicit expression overcomes the limitations of poor interpretability of black-box models. The combination with other

data-driven methods may improve performance.

3 Conclusions

This study presented a computational exploration of the deformation behavior of multiphase CoCrFeNi HEAs, employing an integration of MD simulation and data-driven methods. Tensile experiments were simulated at temperatures of 300, 77, and 4.2 K. Subsequently, a microstructural evolutionary model was established through sparse identification at these temperatures and various tensile rates. Our findings indicate the following:

- (i) The HEAs prepared through melting and quenching exhibited complex multiphase structures characterized by high-density dislocations and some twins, consistent with prior experimental reports.
- (ii) The analysis of the nonatomic packing proportion revealed intense competition among various structures during the initial tensile deformation; the competition gradually stabilized as the deformation progressed. Notably, the disordered structure rapidly increased at the expense of the FCC and HCP structures during the initial plastic stage, followed by mutual rearrangement in the subsequent stage.
- (iii) The extracted model highlighted the leading role of the BCC structure in the evolutionary process and revealed the universal intrinsic mechanism in these scenarios. It has the potential to be applied to other materials and needs to be further investigated.

This work was supported by the National Natural Science Foundation of China (Grant Nos. U23A2065, 52071298, and 51971123) and the National Science Foundation (Grant Nos. DMR-1611180 and 1809640).

Supporting Information

The supporting information is available online at tech.scichina.com and link.springer.com. The supporting materials are published as submitted, without typesetting or editing. The responsibility for scientific accuracy and content remains entirely with the authors.

- 1 Yeh J W, Chen S K, Lin S J, et al. Nanostructured high-entropy alloys with multiple principal elements: Novel alloy design concepts and outcomes. Adv Eng Mater, 2004, 6: 299–303
- 2 Cantor B, Chang I T H, Knight P, et al. Microstructural development in equiatomic multicomponent alloys. Mater Sci Eng-A, 2004, 375: 213–218
- 3 Ren J, Zhang Y, Zhao D X, et al. Strong yet ductile nanolamellar highentropy alloys by additive manufacturing. Nature, 2022, 608: 62–68
- 4 Pan Q S, Zhang L X, Feng R, et al. Gradient cell-structured highentropy alloy with exceptional strength and ductility. Science, 2021, 374: 984–989
- 5 Chen C, Ma L Y, Zhang Y, et al. Accelerating the design of highentropy alloys with high hardness by machine learning based on particle swarm optimization. <u>Intermetallics</u>, 2023, 154: 107819
- 6 Zhang Y, Zuo T T, Tang Z, et al. Microstructures and properties of high-entropy alloys. Prog Mater Sci, 2014, 61: 1–93
- 7 Li J, Fang Q H, Liu B, et al. Transformation induced softening and

- plasticity in high entropy alloys. Acta Mater, 2018, 147: 35-41
- 8 Rao Z Y, Tung P Y, Xie R W, et al. Machine learning-enabled highentropy alloy discovery. Science, 2022, 378: 78–85
- 9 Chang H N, Tao Y W, Liaw P K, et al. Phase prediction and effect of intrinsic residual strain on phase stability in high-entropy alloys with machine learning. J Alloys Compd, 2022, 921: 166149
- 10 Li C H, Wang M L, Zhang H Z, et al. A novel as-cast precipitationstrengthened Al_{0.5}V_{0.1}FeCrMnNi_{0.9} high-entropy alloy with high strength and plasticity. Sci China Tech Sci, 2021, 64: 1920–1926
- 11 Li W D, Xie D, Li D Y, et al. Mechanical behavior of high-entropy alloys. Prog Mater Sci. 2021, 118: 100777
- 12 Guo X X, Xie X, Ren J L, et al. Plastic dynamics of the Al_{0.5}CoCrCuFeNi high entropy alloy at cryogenic temperatures: Jerky flow, stair-like fluctuation, scaling behavior, and non-chaotic state. Appl Phys Lett, 2017, 111: 251905
- 13 Rao Y, Baruffi C, De Luca A, et al. Theory-guided design of highstrength, high-melting point, ductile, low-density, single-phase BCC high entropy alloys. Acta Mater, 2022, 237: 118132
- 14 Chen S, Aitken Z H, Pattamatta S, et al. Short-range ordering alters the dislocation nucleation and propagation in refractory high-entropy alloys. Mater Today, 2023, 65: 14–25
- 15 Ji W M, Wu M S. Nanoscale origin of the crystalline-to-amorphous phase transformation and damage tolerance of Cantor alloys at cryogenic temperatures. Acta Mater, 2022, 226: 117639
- Wang P, Lin Y C, Cao Y, et al. Atomistic simulations of martensitic transformation processes for metastable FeMnCoCr high-entropy alloy. Sci China Tech Sci, 2023, 66: 998–1006
- 17 Li X T, Tang X Z, Guo Y F. Inhibition effect of segregation and chemical order on grain boundary migration in NbMoTaW multiprincipal element alloy. Scripta Mater, 2023, 235: 115632
- 18 Chen S, Wang T, Li X Y, et al. Short-range ordering and its impact on thermodynamic property of high-entropy alloys. Acta Mater, 2022, 238: 118201
- 19 Giwa A M, Aitken Z H, Liaw P K, et al. Effect of temperature on small-scale deformation of individual face-centered-cubic and bodycentered-cubic phases of an Al_{0.7}CoCrFeNi high-entropy alloy. Mater Des, 2020, 191: 108611
- Xiong F, Wu Y, Liu X J, et al. Enhancing cryogenic yield strength and ductility of the Al_{0.1}CoCrFeNi high-entropy alloy by synergistic effect of nanotwins and dislocations. Scripta Mater, 2023, 232: 115495
- 21 Liu J P, Guo X X, Lin Q Y, et al. Excellent ductility and serration feature of metastable CoCrFeNi high-entropy alloy at extremely low temperatures. Sci China Mater, 2019, 62: 853–863
- 22 Vu T N, Pham V T, Fang T H. Influences of grain size, temperature, and strain rate on mechanical properties of Al_{0.3}CoCrFeNi high–entropy alloys. Mater Sci Eng-A, 2022, 858: 144158
- 23 Gao H T, He G Q, Li Q, et al. Diffusion bonding of high entropy alloy and stainless steel at a relative lower temperature via surface nanocrystallization treatment. J Mater Res Tech, 2023, 24: 475–487
- 24 Li J, Chen H T, Li S X, et al. Tuning the mechanical behavior of highentropy alloys via controlling cooling rates. Mater Sci Eng-A, 2019, 760: 359–365
- 25 Sharma A, Balasubramanian G. Dislocation dynamics in Al_{0.1}CoCrFeNi high-entropy alloy under tensile loading. Intermetallics, 2017, 91: 31–34
- 26 Zhang K, Pan S, Tang W, et al. Structural and bonding transformation of Al_{0.67}CrCoCuFeNi high-entropy alloys during quenching. J Alloys Compd, 2018, 753: 636–641
- 27 Kumar S, Pradhan H, Shah N, et al. Machine learning enabled processing map generation for high-entropy alloy. Scripta Mater, 2023, 234: 115543
- Zhang Y P, Chen Z Y, Jin F, et al. Cross-project prediction for rock mass using shuffled TBM big dataset and knowledge-based machine learning methods. Sci China Tech Sci, 2023, 66: 751-770
- 29 Yu L P, Guo X X, Wang G, et al. Extracting governing system for the plastic deformation of metallic glasses using machine learning. Sci China-Phys Mech Astron, 2022, 65: 264611

- 30 Wei G Y, Cui J Z, Wang W, et al. Short-to-medium range structure and glass-forming ability in metallic glasses. Phys Rev Mater, 2022, 6: 055601
- 31 Wu L L, Wei G Y, Wang G, et al. Creating win-wins from strength-ductility trade-off in multi-principal element alloys by machine learning. Mater Today Commun, 2022, 32: 104010
- 32 Chen C, Zhou H R, Long W M, et al. Phase prediction for highentropy alloys using generative adversarial network and active learning based on small datasets. Sci China Tech Sci, 2023, 66: 3615– 3627
- 33 Brunton S L, Proctor J L, Kutz J N. Discovering governing equations from data by sparse identification of nonlinear dynamical systems. Proc Natl Acad Sci USA, 2016, 113: 3932–3937
- 34 Plimpton S. Fast parallel algorithms for short-range molecular dynamics. J Comput Phys, 1995, 117: 1–19
- 35 Farkas D, Caro A. Model interatomic potentials and lattice strain in a high-entropy alloy. J Mater Res, 2018, 33: 3218–3225
- 36 Yan S H, Qin Q H, Zhong Z. On the real-time atomistic deformation of nano twinned CrCoFeNi high entropy alloy. Nanotechnology, 2020, 31: 385705
- 37 McCarthy M J, Zheng H, Apelian D, et al. Emergence of near-boundary segregation zones in face-centered cubic multiprincipal element alloys. Phys Rev Mater, 2021, 5: 113601
- 38 Zhang C, Zhu J K, Ji C Y, et al. Laser powder bed fusion of high-

- entropy alloy particle-reinforced stainless steel with enhanced strength, ductility, and corrosion resistance. Mater Des, 2021, 209: 109950
- 39 Feng H, Cui S Y, Chen H T, et al. A molecular dynamics investigation into deformation mechanism of nanotwinned Cu/high entropy alloy FeCoCrNi nanolaminates. Surf Coatings Tech, 2020, 401: 126325
- 40 Larsen P M, Schmidt S, Schiøtz J. Robust structural identification via polyhedral template matching. Model Simul Mater Sci Eng, 2016, 24: 055007
- 41 Stukowski A, Albe K. Extracting dislocations and non-dislocation crystal defects from atomistic simulation data. Model Simul Mater Sci Eng., 2010, 18: 085001
- 42 Stukowski A. Visualization and analysis of atomistic simulation data with OVITO-the Open Visualization Tool. Model Simul Mater Sci Eng, 2010, 18: 015012
- 43 Zhou Z K, Guo Z F, Johnson W L, et al. Crystal-to-glass transition in multicomponent alloys under high strain rates. Acta Mater, 2023, 258: 119233
- 44 Honeycutt J D, Andersen H C. Molecular dynamics study of melting and freezing of small Lennard-Jones clusters. J Phys Chem, 1987, 91: 4950–4963
- 45 Huo W Y, Zhou H, Fang F, et al. Strain-rate effect upon the tensile behavior of CoCrFeNi high-entropy alloys. Mater Sci Eng-A, 2017, 689: 366–369